Volume 14, Issue 2, 142409 (1-12)

Iranian Journal of Catalysis (IJC)

https://doi.org/10.57647/j.ijc.2024.1402.09

Photocatalytic degradation of methylene blue through carbon dot-doped and amino-functionalized ZIF-8

Qi Zhang, Lu Zhang, Xianglin Cheng*, Jinna Li, Ziyi Qi

Zhengzhou University, Henan Province, China.

***Corresponding authors:** cxl8817@163.com

Original Research

Received:
4 January 2024
Revised:
27 February 2024
Accepted:
25 May 2024
Published online:
31 May 2024

Abstract:

In this paper a one-step synthesis method to prepare NH_2-ZIF-8/NCDs porous materials is introduced. A series of composite photocatalysts were obtained by adjusting the additional amount of nitrogen-doped carbon quantum dots (NCDs). The structural characteristics of the nanocomposites were characterized using XRD, FTIR, FESEM, TEM, and BET. The photocatalytic activity of NH_2-ZIF-8/NCDs nanocomposites was investigated through the photocatalytic degradation of methylene blue (MB). The results show that when the addition amount of ethylenediamine and NCDs is 1:5, the prepared NH2-ZIF-8/NCDs catalyst can degrade 76.2% of the 20 mg/L methylene blue (MB) solution within 5 minutes of illumination. 97.1% of MB was degraded after 60 minutes. The photocatalytic activity of NH2-ZIF-8/NCDs photocatalyst is higher than that of ZIF-8 and ZIF-8/NCDs photocatalyst. Free radical capture experiments showed that hydroxyl radicals (·OH) were the main active species responsible for removing MB under light illumination.

Keywords: Degradation; Methylene blue; NH_2-ZIF-8/NCDs porous materials; Photocatalysis; ZIF-8

1. Introduction

The textile industry is constantly evolving, and the use of dyes is increasing daily. While dyes bring convenience to people's lives, they also cause water pollution. In order to reduce the harm caused by dyes to the environment, people have adopted various methods to decolorize and degrade industrial dye wastewater [1, 2]. Such as adsorption, filtration, membrane technology, coagulation, electrochemical oxidation and photocatalytic degradation, etc.

Among them, photocatalytic degradation technology is a green, environmentally friendly, low-cost, and high-degradation efficiency method. It has significant advantages over other methods in solving environmental pollution and other problems and is considered an effective strategy to reduce wastewater pollution. When the photocatalyst is irradiated by light with energy greater than or equal to the band gap, the electrons in its valence band (VB) will be excited to transition to the conduction band (CB), leaving relatively stable holes (h^+) in the VB, thus forming electron-hole pairs (e^--h^+). The large number of defects present in the photocatalyst can effectively capture e^--h^+ and prevent their recombination. These captured e^--h^+ diffuse to the surface of the particles respectively, thereby generating a strong redox potential and further degrading the target organic matter [3, 4].

Since the widespread application of photocatalytic degradation, various types of photocatalysts have emerged for catalysis [5–7]. Metal-organic framework (MOF), as a new type of porous solid material, has efficient and adjustable photoluminescence performance, high specific surface area, various types of adjustable pore sizes, and stable chemical properties [8–11]. ZIF-8 has become a research hotspot in water pollution treatment [12–15]. In 2014, Wang et al. reported [16] that ZIF-8 photocatalyst can degrade and adsorb MB under ultraviolet light irradiation and is a potential photocatalyst for degrading organic pollutants. However, some studies have shown [10–15] that ZIF-8 can only produce activating substances through ultraviolet irradiation, and the content of the generated activating substance is relatively low, making it easy for electrons and holes to recombine during the photocatalytic process. Therefore, to achieve

better catalytic effect, it is necessary to modify or dope the original ZIF-8 material [14, 17–19]. Improve photocatalytic efficiency by changing their structure, adjusting their morphology, engineering their surfaces and interfaces, and engineering their surfaces and defects [20]. For example, Santos et al. [21] synthesized ZIF-8 in situ in the presence of sodalite zeolite (SOD) to obtain a heterostructured ZIF-8/SOD photocatalyst with a larger surface area and diverse pore distribution. This structure has It is beneficial to increase the contact with the photocatalyst, thereby promoting effective photocatalytic degradation, making its degradation rate of ciprofloxacin antibiotics up to 98%. Therefore, to enhance the catalytic activity of ZIF-8, one potential approach is to functionalize it with materials that can modify its surface properties. Carbon dots (CDs) are one such material that could be considered for this purpose. CDs are carbon analogs with unique optical properties, which, when combined with some metal oxides or semiconductors, can make the heterojunction exhibit good optical properties [22–24]. Jayasree et al. [25] successfully encapsulated NCDs into ZIF-8 by solvothermal method and characterized the resulting catalyst. Khalk et al. [26] used NCDs doped with ZIF-8 to degrade methylene blue. Although it has a certain degradation efficiency compared to ZIF-8, the degradation efficiency of NCDs and ZIF-8 composite catalysts is not high, and further modification is needed to improve their photodegradation efficiency.

In this study adopts a one-step synthesis method to prepare NH_2-ZIF-8/NCDs photocatalyst by modifying ZIF-8 with ethylenediamine and adding NCDs for loading. The introduction of NH_2 groups is expected to change the morphology of ZIF-8 into a loose and porous structure to increase the reaction sites of the catalyst, where more NCDs can be modified to obtain better optical properties. The obtained NH_2-ZIF-8/NCDs photocatalyst was used to degrade methylene blue.

2. Experimental

2.1 Materials

Zinc acetate hexahydrate, 2-methylimidazole, methanol, ethanolamine, 30% hydrogen peroxide, and ethylenediamine are all from Tianjin Comeo Chemical Reagent Co. Ltd., and all chemicals are analytical grade, used without any further purification.

2.2 Sample preparation

2.2.1 Preparation of NCDs

The process of preparing NCDs has been improved based on the literature [27]. 30 mL of ethanolamine and 45 mL of 30% hydrogen peroxide were added into a 1 L beaker, mixed evenly, and placed in a preheated oven at 180 °C. After the solution completely changed into a brown viscous fluid, the beaker was taken out and cooled to room temperature. The product was subjected to ultrasound and washed with ethanol repeatedly. During the washing process, the ethanol solution turned yellow, indicating the dissolution of organic impurities. After the solution was washed to colorless, the resulting solid was vacuum dried at 60 °C to obtain NCDs powder.

2.2.2 Preparation of ZIF-8

First, 1.48 g of zinc nitrate hexahydrate was dissolved in 50 mL methanol (solution A), and second, 1.64 g of 2-methylimidazole was dissolved in another 50 mL methanol (solution B). Then, solution A was slowly poured into solution B and stirred for 2 hours. Subsequently, the stirred solution was kept for 12 hours for aging treatment. The obtained white solid precipitate was washed three times with methanol and distilled water and then dried for 10 hours in a vacuum drying oven at 60 °C to obtain ZIF-8 powder. The preparation method was similar to that in the literature [28].

2.2.3 Preparation of ZIF-8/NCDs

On the basis of preparing ZIF-8, add different volumes of NCDs solutions (1 mg/mL) to solution B, and then perform the same operation as ZIF-8 to obtain ZIF-8/NCDs catalysts with different amounts of NCDs added.

2.2.4 Preparation of NH_2-ZIF-8/NCDs

Based on preparing ZIF-8, after adding different proportions of NCDs and Ethylenediamine into solution B, the following operations were carried out to obtain different proportions of NH_2-ZIF-8/NCDs (1: X).

2.3 Characterization

In order to determine the crystal structure of the prepared samples, this experiment used the Panalytical Empyrean model instrument produced by Panalco in the Netherlands for X-ray diffraction (XRD) testing. The specific scanning angle range was 5-50° and the scanning speed was 5°/meter. The ThermoScientific NicoletiS20 FTIR spectrometer produced by Thermo Fisher Scientific was used to test and analyze the functional groups of the photocatalyst. The spectra were recorded in the transmission mode from 4000∼500 cm^{-1}.

The X-ray photoelectron spectroscopy (XPS) test was carried out using the model Thermo Scientific K-Alpha$^+$ instrument produced by Thermo Fisher Scientific in the United States, and the binding energy was calibrated using the C1s peak of 284.6 eV as the benchmark.

Scanning Electron Microscope (SEM) imaging was carried out using the model ZEISSGemini300 instrument produced by Zeiss in Germany to observe the microscopic morphology of the photocatalyst.

Nitrogen adsorption-desorption measurements were performed using the Brunauer-Emmet-Teller (BET) method on the belsorp-miniII analyzer.

UV-visible diffuse reflectance spectroscopy (UV-VIS DRS) was performed on a Jasco V-750 instrument equipped with integrating spheres.

Electrochemical impedance spectroscopy (EIS) and transient photocurrent (PC) data graphs of the catalyst were obtained using the CHI660E electrochemical workstation. Na_2SO_4. (0.5M) aqueous solution was used as the electrolyte. On a fluorine-doped tin oxide-coated glass plate (FTO), a material with a solution content of 20 μL was dispersed in a defined area of 0.5 cm^2, and the photocurrent was measured. Afterward, the device was immersed in an electrolyte that was previously purified with nitrogen

to remove dissolved oxygen, and the applied potential and wavelength were 0.9 V and 368 nm, respectively. Pt foil was used as the counter electrode, Ag/AgCl (saturated) was used as the reference electrode, and the sample was used as the working electrode.
Transmission microscopy (TEM) was performed on a high-resolution electron microscope type, FEITecnaiG2F20, in the Netherlands.

2.4 Adsorption and photocatalytic experiments

The photocatalytic degradation experiment was performed in a 150 mL photochemical reactor equipped with a xenon lamp (λ >380 nm). The reactor was placed under the xenon lamp, which simulated the light. For each experiment, the photocatalyst powder was accurately weighed, and 100 mL of MB aqueous solution (20 mg/L) was poured into the photoreactor. The stirring speed was 800 rpm. Before light irradiation, the suspension was magnetically stirred in the dark for 30 minutes to achieve adsorption-desorption equilibrium between organic molecules and the photocatalyst surface. After turning on the xenon light source, about 5 mL of suspension was drawn from the reactor at specific times, and the catalyst particles were filtered with a 0.22 μm membrane filter to obtain the supernatant for analysis. The concentration of the MB target pollutant was determined at the maximum absorption wavelength (664 nm) by ultraviolet-visible spectrophotometer, and the degradation rate of the catalyst was calculated [29].
The degradation rate of MB by the catalyst is calculated as follows:

$$C/C_0 = A/A_0$$
$$\eta = (1 - A_t/A_0) \times 100\%$$

In the formula, C_0 (mg/mL) and C (mg/mL) are the initial concentration and real-time concentration of MB in the solution, respectively, and A_0 and A are the initial and real-time absorbance of the solution, respectively. η is the photocatalytic degradation rate of composite materials in %; A_0 is the initial concentration of MB in mg/L; A_t is the MB concentration at different time intervals in mg/L.
In order to determine the active substances of photocatalytic degradation of organic pollutants, further radical trapping experiments were conducted. Tert-butyl alcohol, methanol, and p-benzoquinone were added to the 20 mg/L methylene blue (MB) reaction solution for scavenging hydroxyl radicals, holes, and electrons, respectively. The experimental steps are the same as reported in the literature. The optimal reaction ratio of photocatalysts is obtained by changing factors such as the synthesis ratio of photocatalysts, the amount of photocatalysts, and the type of catalysts [30].
Standard Curve: A stock solution (25 mg/mL) was obtained by dissolving 25 mg of MB in water and fixing the solution with deionized water in a 250 mL volumetric flask. The stock solution was diluted to obtain aqueous MB solutions of 2, 4, 6, 8, and 10 mg/mL, respectively. The absorbance was then analyzed using a UV-Vis spectrometer at a maximum wavelength of 665 nm.

3. Results and discussion

3.1 Structural properties

3.1.1 XRD

Fig. 1 shows the XRD data of ZIF-8, ZIF-8/NCDs, and NH_2-ZIF-8/NCDs. In the XRD pattern of ZIF-8, obvious diffraction peaks were observed in the range of 5 50°, corresponding to (011), (002), (112), (022), (013), and (222) crystal planes which were consistent with the simulated pattern from CCDC 287180 [31, 32], indicating that the synthesized ZIF-8 has high crystallinity. Compared with pure ZIF-8, the XRD patterns of ZIF-8/NCD and NH_2-ZIF-8/NCDs have no obvious changes except that the peak density becomes stronger, indicating that the modification of ethylenediamine and the loading of NCDs did not produce new phases [33].

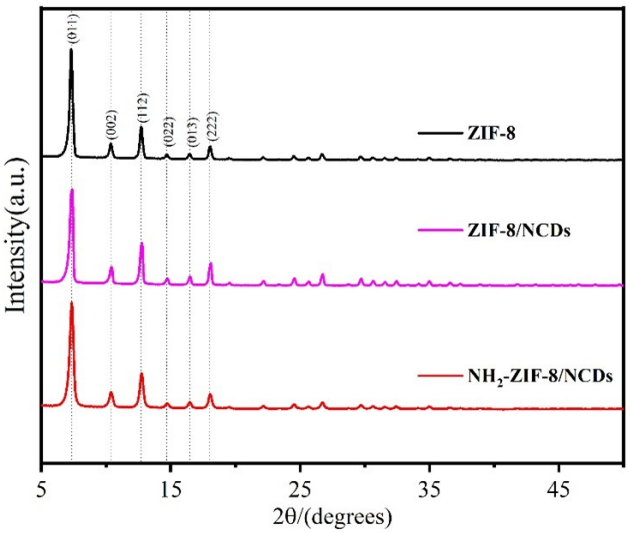

Figure 1. XRD patterns of ZIF-8, ZIF-8/NCDs, and NH_2-ZIF-8/NCDs.

3.1.2 FTIR

The surface functional groups present on ZIF-8, ZIF-8/NCDs, and NH_2-ZIF-8/NCDs composites were identified by FTIR spectra. As shown in Fig. 2a, the absorption peaks appear at 752, 996, 1146, 1306, 1427, 1587, 2928, and 3143 cm^{-1} on the surfaces of catalysts of ZIF-8, ZIF-8/NCDs and NH_2-ZIF-8/NCDs. The absorption peaks at 752, 1146, and 1306 cm^{-1} are due to the bending vibration of the imidazole ring, while the absorption peak at 1423 cm^{-1} is due to the stretching vibration of the imidazole ring [34]. The vibration band at 1587 cm^{-1} is attributed to the stretching of the N-H bond [35]. Also, the diffraction peak of NH_2-ZIF-8/NCDs is more prominent due to the addition of ethylenediamine, proving the successful addition of ethylenediamine. In addition, the characteristic peak at 3520 cm^{-1} is caused by the stretching vibration of -OH. The prepared NCDs have a large number of surface hydroxyl groups (as shown in Fig. 2b) and are easily soluble in water [36]. It is precisely due to the addition of ethylenediamine and NCDs that the imidazole ring is partially replaced during the synthesis

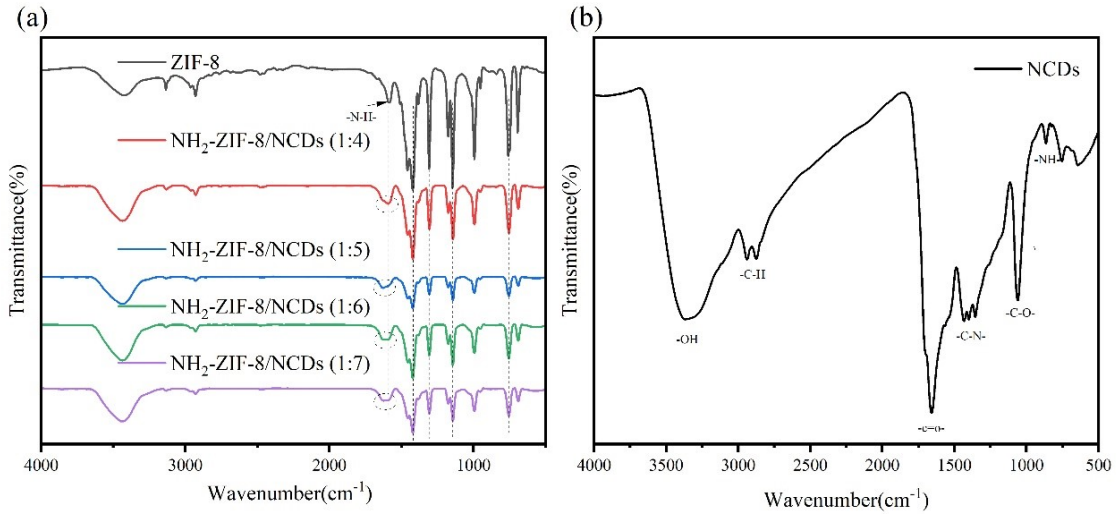

Figure 2. FTIR spectra of ZIF-8,and NH_2-ZIF-8/NCDs samples between 4000 cm^{-1} -500 cm^{-1} (a) and FTIR spectra of NCDs (b).

process, and the diffraction peak corresponding to ZIF-8 is relatively weakened.

3.1.3 XPS

In order to further prove the successful introduction of ethylenediamine and doping of carbon points in the framework of ZIF-8, X-ray photoelectron spectroscopy (XPS) analysis was performed on ZIF-8 and NH_2-ZIF-8/NCDs and the chemical bonding states of N in ZIF-8 and NH_2-ZIF-8/NCDs were detected. As shown in Fig. 3, there are two corresponding peaks of Zn-N (398.5 eV), and 2-methylimidazole (400.5 eV) in pure ZIF-8 [36]. In contrast, ZIF-8/NCDs and NH2-ZIF-8/NCDs added N-C-O peaks and N-H peaks to the original peaks of ZIF-8 (23), and the appearance of N-C-O peaks indicated the successful loading of NCDs. Comparing the peaks of N-H and Zn-N in the N1s spectrum of ZIF-8/NCDs, it can be found that the peak of NH in NH_2-ZIF-8/NCDs is higher than that of ZIF-8/NCDs, while the peak of Zn-N is lower than ZIF-8/NCDs. This phenomenon may occur because the addition of ethylenediamine causes partial collapse of the ZIF-8 skeleton. During the reaction, substituted Zn (II) combines with 2-methylimidazole.

3.2 Surface Morphology

3.2.1 SEM

The morphology of ZIF-8, ZIF-8/NCDs, and NH_2-ZIF-8/NCDs composites was studied by scanning electron microscopy (SEM), as shown in Fig. 4a-c. Fig. 4a is the SEM image of ZIF-8, showing the morphology consistent with that commonly observed in the literature [37]. ZIF-8 has a uniform rhombic dodecahedron shape with an average diameter of 200 nm. By comparing the SEM image of ZIF-8/NCDs composite with that of ZIF-8, it was found that the external morphology of ZIF-8/NCDs composite was not significantly different from that of ZIF-8, indicating that the simple introduction of NCDs would not change the original structure of ZIF-8. However, some NCDs attached to the surface of ZIF-8 can be observed in Fig. 4b, proving that NCDs modify ZIF-8. By observing the SEM image of NH_2-ZIF-8/NCDs (Fig. 4c), it can be found that the morphology of NH_2-ZIF-8/NCDs has undergone great changes. It shows a loose porous network structure instead of a cube structure, which may be caused by adding ethylenediamine to change its original structure.

According to the EDS element mapping diagram (Fig. 4d), it can be determined that NH_2-ZIF-8/NCDs contain C, O,

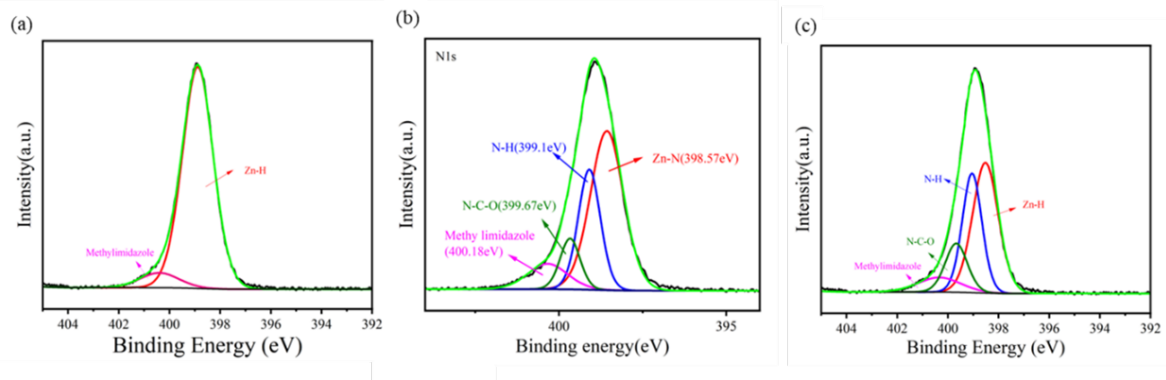

Figure 3. XPS spectra of N1s for ZIF-8 (a), ZIF-8/NCDs (b) and NH_2-ZIF-8/NCDs (c).

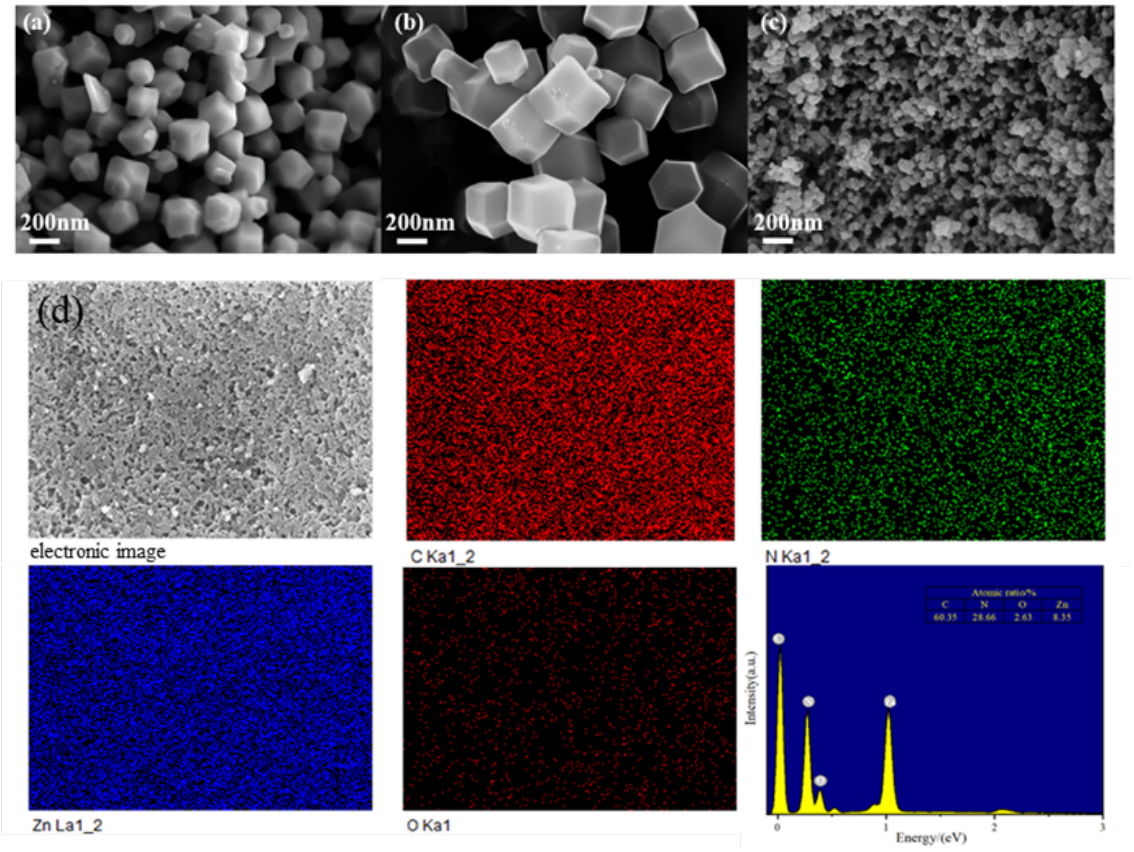

Figure 4. SEM images of the ZIF-8 (a), ZIF-8/NCDs (b), NH_2-ZIF-8/NCDs (c), element mapping of NH_2-ZIF-8/NCDs composite and EDS pattern of the NH_2-ZIF-8/NCDs (d).

N, Zn, and other elements and show a uniform distribution. Among them, the atomic contents of C, O, N, and Zn were 60.35%, 28.66%, 2.63%, and 8.35%, respectively.

3.2.2 TEM

Fig. 5 shows the TEM images of NCDs and NH_2-ZIF-8/NCDs, as shown in the figure. Fig. 5a-b are TEM images of the prepared NCDs, in which it can be seen that the carbon points are approximately circular and evenly distributed [38]. After the Fourier transform is performed on their lattice fringes, it can be seen that their lattice spacing is 0.24nm, corresponding to the (100) crystal plane structure of graphite [39]. In Fig. 5c-d are TEM images of NH_2-ZIF-8/NCDs; it can be seen that NCDs is uniformly loaded on the catalyst.

3.2.3 BET

The textural properties of the synthesized materials were evaluated by nitrogen adsorption-desorption isotherms at -196 °C (Fig. 6). As can be seen from Fig. 6a, both ZIF-8, and ZIF-8/NCDs exhibit typical type I adsorption isotherms according to the IUPAC classification, which is characteristic of microporous materials [40]. On the other hand, NH_2-ZIF-8/NCDs exhibit type IV isotherms characteristic of mesoporous pores. As can be seen from Fig. 6b, there are differences in pore size and distribution of different samples, and NH_2-ZIF-8/NCDs structure has a larger pore volume and wider pore size distribution than ZIF-8 and ZIF-8/NCDs materials. The large pore size range of NH_2-ZIF-8/NCDs material structure is conducive to the mass transfer rate of pollutant molecules and improves the efficiency of the

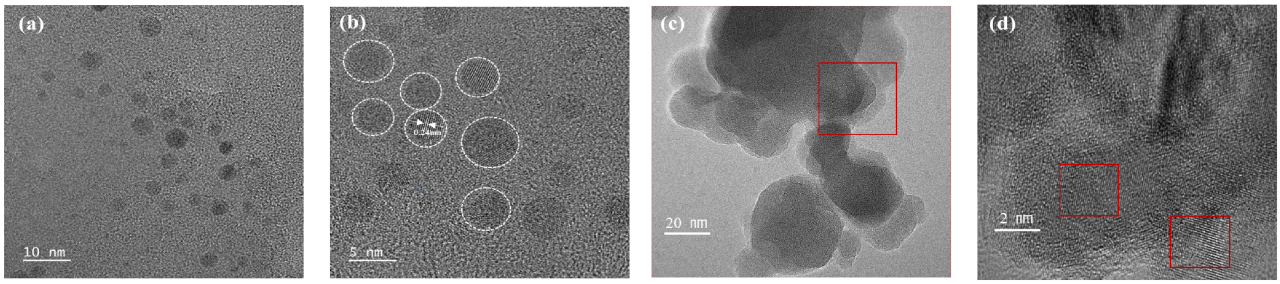

Figure 5. HR-TEM images of NCDs (a-b) and NH_2-ZIF-8/NCDs(c-d).

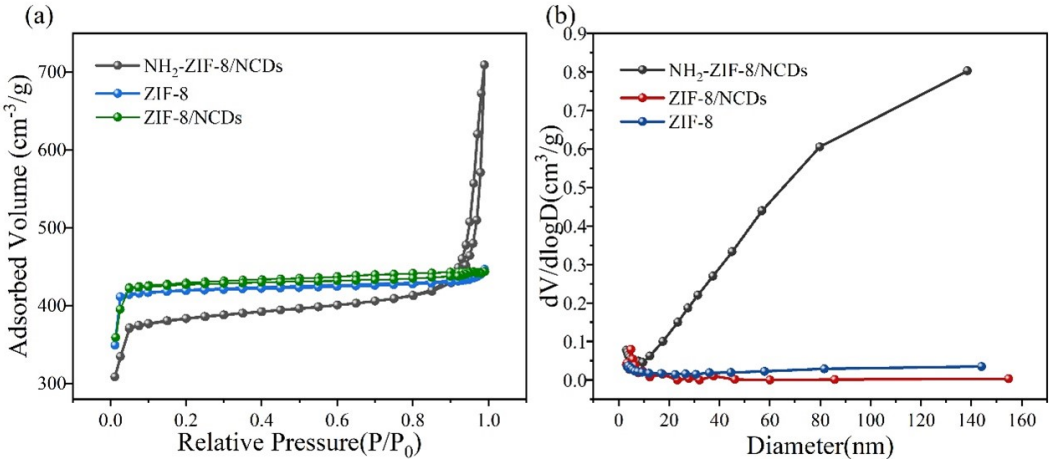

Figure 6. Nitrogen adsorption-desorption isotherms (a) and pore size distribution (b) for ZIF-8, ZIF-8/NCDs, and NH_2-ZIF-8/NCDs.

material as a photocatalyst.

3.3 Optical properties

3.3.1 DRS

The optical absorption characteristics of ZIF-8, ZIF-8/NCDs, and NH_2-ZIF-8/NCDs materials were measured by UV visible diffuse reflectance spectroscopy (DRS) at room temperature, as shown in Fig. 7. Fig. 7a shows that the optical response of ZIF-8, ZIF-8/NCDs, and NH_2-ZIF-8/NCDs materials is mostly concentrated at wavelengths below 250 nm. However, local enlargement (Fig. 7b) shows that the absorption edge of ZIF-8/NCDs is similar to that of ZIF-8. However, a small absorption peak can be observed near 275-400 nm in ZIF-8/NCDs. This peak may be due to carbon dots doping in the ZIF-8/NCDs sample and the production of a certain amount of photogenerated carriers, increasing the optical absorption [32]. A high absorption peak can be observed in the NH_2-ZIF-8/NCDs catalyst between 400 nm and 700 nm, and there is a varying degree of redshift at the absorption edge, indicating that the amination of ZIF-8 and the doping of carbon dots can greatly improve the light absorption efficiency. Improving light absorption performance can accelerate the photocatalytic degradation efficiency of NH_2-ZIF-8/NCDs composite material under visible light. The optical band gap of each catalyst can be determined by applying Kubelka-Munk theory. By plotting $(ahn)^2$ vs. $h\upsilon$, where a represents the absorption coefficient, and h stands for photon energy, the band gap widths of ZIF-8, ZIF-8/NCDs, and NH_2-ZIF-8/NCDs are measured to be 5.21 eV, 5.20 eV, and 5.14 eV, respectively, as illustrated in Fig. 8.

3.3.2 photocurrent testing

The effect of NH_2-ZIF-8/NCDs composite material on promoting carrier separation was studied through photocurrent testing, as shown in Fig. 9. The photocurrent time curves of ZIF-8, ZIF-8/NCDs, and NH_2-ZIF-8/NCDs under six on/off cycles are studied. Fig. 9a shows that all samples can be excited to generate photocurrent under simulated sunlight exposure. The photoelectric response of NH_2-ZIF-8/NCDs is significantly higher than that of ZIF-8/NCDs and ZIF-8, indicating that the porous structure of NH_2-

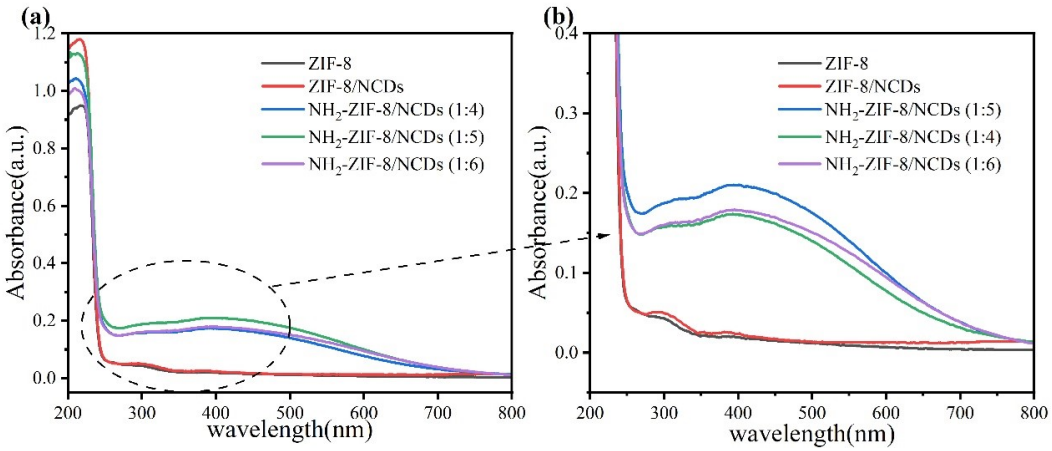

Figure 7. DRS spectra (a) of ZIF-8, ZIF-8/NCDs, and NH_2-ZIF-8/NCDs composites; Partial magnification (b) of the DRS spectrum.

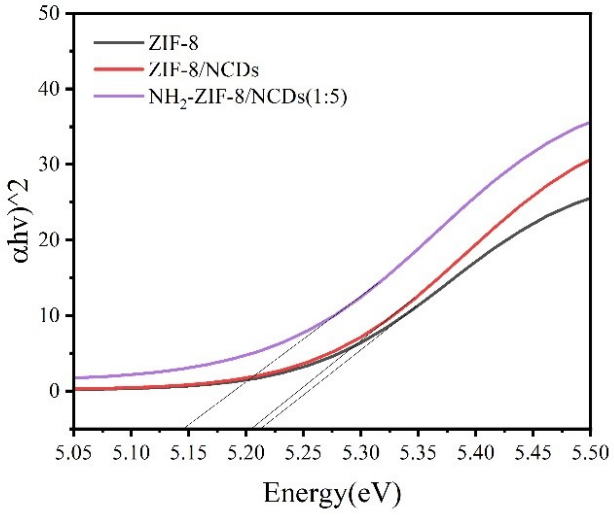

Figure 8. The variation curve of $(\alpha h\upsilon)^2$ with photon energy of photocatalyst.

ZIF-8/NCDs composite improves carrier separation and increases photocurrent. At the same time, electrochemical impedance spectroscopy (EIS) experiments were also conducted. Overall, the smaller the arc radius, the faster the interface transfer and the higher the electron-hole separation efficiency [41]. The data in Fig. 9b shows that ZIF-8 has the largest arc radius, while NH_2-ZIF-8/NCDs have the smallest arc radius. The results indicate that NH_2-ZIF-8/NCDs porous composite materials have lower carrier transport resistance and higher charge transfer efficiency than ZIF-8 and ZIF-8/NCDs. The above observations emphasize the outstanding performance of NH_2-ZIF-8/NCDs catalysts in separating electron-hole pairs. The results are consistent with the degradation experiment.

3.4 Photocatalytic activity experiment

3.4.1 Photocatalytic performance and stability investigation

The photocatalytic activity of ZIF-8, ZIF-8/NCDs, ZIF-8/NCDs, and NH_2-ZIF-8/NCDs was investigated by observing the degradation effect of MB under light. Fig. 10 shows the degradation effect of each catalyst on MB under light and compares the kinetic efficiency of the photocatalytic reaction. After stirring in the dark for 30 min, MB and the catalyst reached the adsorption-desorption equilibrium, and the photocatalytic degradation experiment was carried out. It can be seen from Fig. 10a that the adsorption capacity of ZIF-8 to MB dye solution is weak, and the photocatalytic activity is also low. The degradation rate of ZIF-8 was 48% under 60 min of light irradiation and only 61.2% under 120 min of light irradiation. The degradation rate of ZIF-8/NCDs reached 92.4% under 120 min illumination, and the photocatalytic performance was improved. On this basis, the photocatalyst NH_2-ZIF-8/NCDs obtained by amine-group modification reached the degradation rate of 76.2% within 5 min illumination. The degradation rate reached 97.1% after 60 min illumination. By comparing the degradation efficiency of the NH_2-ZIF-8 catalyst, it can be seen that the synergistic effect of carbon point doping and amine group modification can play a better role in photo-

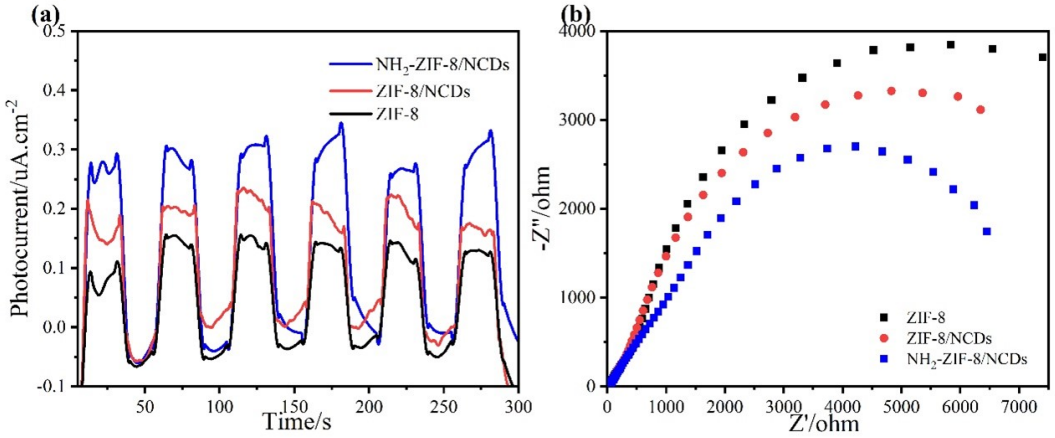

Figure 9. Transient photoelectric current response (a) and EIS (b) of ZIF-8, ZIF-8/NCDs, and NH_2-ZIF-8/NCDs composite.

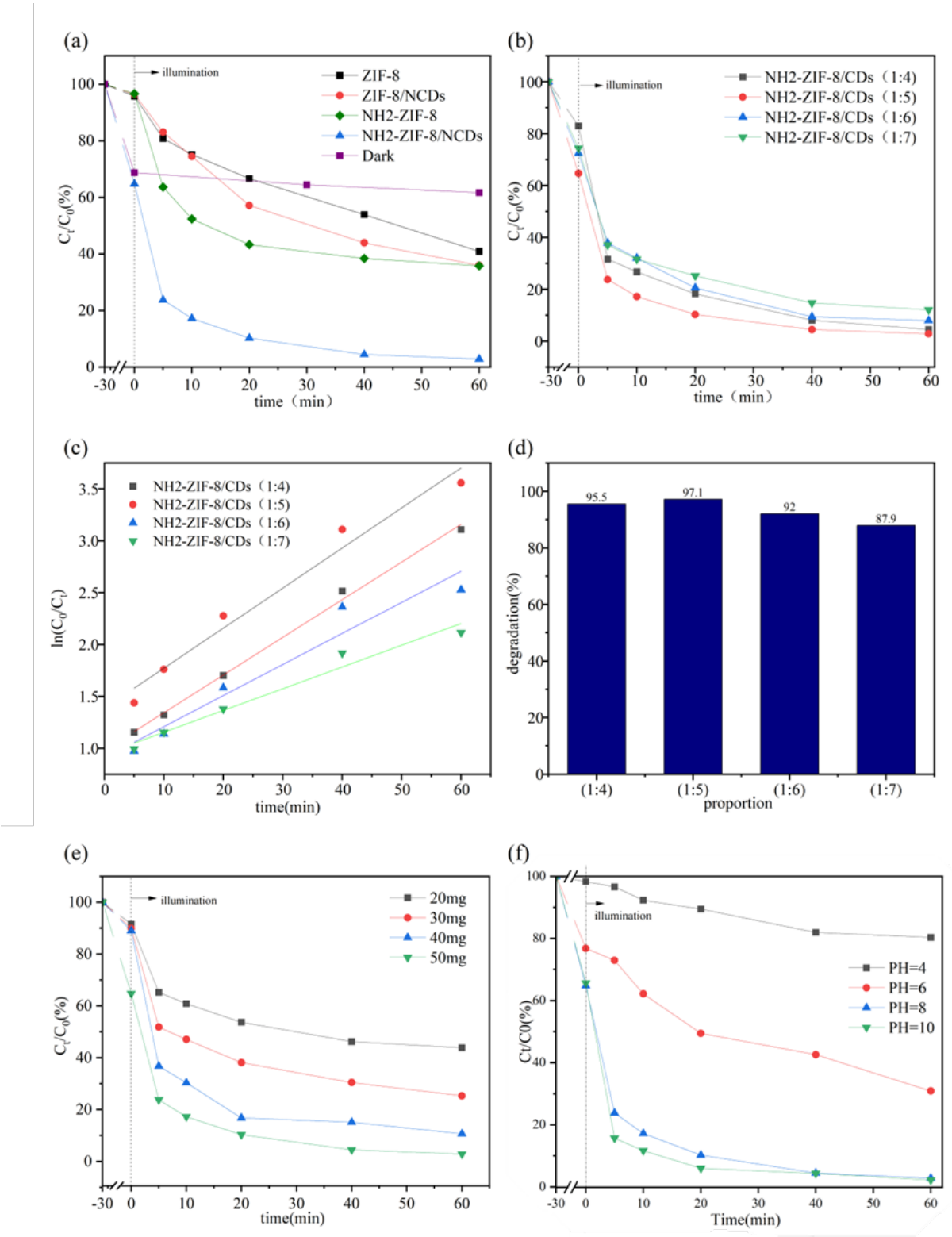

Figure 10. The photocatalytic reaction conditions in this figure are all 30 minutes under dark conditions, followed by degradation of MB solution (20 mg/L) under xenon lamp irradiation. Photocatalytic degradation efficiency (a) of ZIF-8, ZIF-8/NCDs, NH_2-ZIF-8 and NH_2-ZIF-8/NCDs (1:5) composites on MB solution (20mg/L). Photocatalytic degradation efficiency (b) of NH_2-ZIF-8/NCDs(1:4,1:5,1:6,1:7) composites in MB solution (20mg/L) and its relationship between ln C/Co and Time relationship (c). Comparison of degradation rates (d) of NH2-ZIF-8/NCDs (1:4, 1:5, 1:6, 1:7). Comparison of the degradation efficiency (e) of NH_2-ZIF-8/NCDs (1:5) with different masses on MB solution (20mg/L). Effect of pH on photodegradation efficiency of NH2-ZIF-8/NCDs photocatalyst(f).

catalysis. Compared with the first two catalysts, the degradation efficiency of NH_2-ZIF-8/NCDs is 12 times higher than that of ZIF-8 under the same illumination time. When the degradation rate reaches around 95%, the NH_2-ZIF-8/NCDs catalyst takes half less time than the ZIF-8/NCDs catalyst. In order to eliminate experimental contingency, the above catalyst degradation experiments were repeated multiple times, and the degradation efficiency was averaged to prove the accuracy of the experiments. Finally, it is proved that the NH_2-ZIF-8/NCDs catalyst obtained by compounding ZIF-8 with aminoation and carbon dot doping has better photocatalytic performance than ZIF-8 and ZIF-8/NCDs. Moreover, after the MB solution containing NH_2-ZIF-8/NCDs photocatalyst was exposed to light for 60 min, the NH_2-ZIF-8/NCDs catalyst was filtered out and continued to be exposed to light for 30 min. The degradation rate of MB was not significantly reduced at this stage, indicating that the catalyst-free MB solution was stable under light. The degradation of NH_2-ZIF-8/NCDs in MB solution is heterogeneous catalysis. In order to eliminate the influence of surface adsorption, NH_2-ZIF-8/NCDs photocatalyst was added to the MB solution (20 mg/L) and stirred for 90 minutes in the dark. The results showed that the photocatalyst could reach adsorption equilibrium within 30 minutes. After stirring for 90 minutes, the concentration of the MB solution did not decrease significantly. The results can be seen in Fig. 10a.

Different NH_2-ZIF-8/NCDs (1:X) photocatalysts were obtained by adjusting the ratio of carbon dots and amine groups, and their photocatalytic effects were studied to see if they were different. As shown in Fig. 10b, the degradation rates of MB by NH_2-ZIF-8/NCDs (1:4), NH_2-ZIF-8/NCDs (1:5), NH_2-ZIF-8/NCDs (1:6), and NH_2-ZIF-8/NCDs (1:7) were 95.5%, 97.1%, 92.0%, 92.74% and 87.9% after 60 min of light irradiation. When the ratio of NH_2-ZIF-8/NCDs is 1:5, the photocatalytic degradation efficiency is the highest. As the content of carbon dots in NH_2-ZIF-8/NCDs increases to a certain extent, the photocatalytic activity of the composite material decreases. This phenomenon may be due to the fact that when excessive carbon dot nanoparticles are combined with ZIF-8, the carbon dots wrap around ZIF-8 and hinder its active site. In this case, the contact area between the composite material and MB dye decreases, thereby reducing photocatalytic activity. Therefore, only an appropriate proportion of NH_2-ZIF-8/NCDs can maximize the photocatalytic degradation ability. The catalytic activity of the sample was further evaluated using a pseudo-first-order kinetics model to fit degradation data and the photocatalytic degradation rate constant. Fig. 10c shows the ln (C_0/C_t) variation curve with time t. It can be observed that the decolorization rate of MB always follows the quasi-first order kinetic equation, and the photocatalytic degradation rate K can be calculated via the linear fitting equation [32]. The corresponding rate constants k for NH_2-ZIF-8/NCDs (1:4), NH_2-ZIF-8/NCDs (1:5), NH_2-ZIF-8/NCDs (1:6), and NH_2-ZIF-8/NCDs (1:7) are 0.03633 min^{-1}, 0.03862 min^{-1}, 0.02996 min^{-1}, and 0.02095 min^{-1}, respectively. The kinetic rate constants and R2 of each catalyst for MB solution (20 mg/L) can be seen in Table 1. The amount of catalyst also affects the photocatalytic degradation rate. As shown in Fig. 10e, when the mass of NH_2-ZIF-8/NCDs (1:5) photocatalysts is 20 mg, 30 mg, 40 mg, and 50 mg, they have different degradation efficiency. Under 60 minutes of light irradiation, their degradation rates are 56.2%, 74.7%, 89.4%, and 97.1%, respectively.

The pH value of the solution is a crucial factor in the photocatalytic degradation process. To explore the impact of pH on both the adsorption capacity and degradation efficiency of MB solution in photocatalytic experiments, the pH levels were adjusted to 4, 6, 8, and 10 using HCl or NaOH solutions. NH_2-ZIF-8/NCDs (1:5) was utilized as the experimental photocatalyst to assess its adsorption and degradation efficiency for MB solution. As depicted in Fig. 10f, an increase in pH led to a gradual enhancement in both the adsorption capacity and catalytic efficiency of the catalyst towards the MB solution. In an alkaline setting, NH_2-ZIF-8/NCDs exhibited robust adsorption capabilities towards the MB solution, possibly due to the attraction between the negatively charged catalyst and the positively charged MB solution. Enhanced adsorption could potentially improve degradation efficiency. The increased OH- concentration may be the reason for the high degradation efficiency of the MB solution, because OH- can neutralize the H+ produced by photocatalysis, thus promoting the progress of photocatalysis [16]. In order to evaluate the stability and reusability of the material, we conducted photocatalytic cycle experiments on the NH_2-ZIF-8/NCDs photocatalyst under the same degradation conditions. After each photodegradation experiment, the photocatalysts were collected by centrifugation. After drying, the next photocatalytic experiment was carried out and repeated three times. The photocatalytic cycle experimental results were obtained, as shown in Fig. 11. It can be seen from the results that due to the inevitable loss of the catalyst during the recycling process, the removal rate of MB has decreased after three cycles, dropping to 81.6%. However, in comparison, it still has good photocatalytic activity. The results show that the NH_2-ZIF-8/NCDs photocatalyst has good reusability.

As shown in Fig. 12, the absorption spectrum of the MB solution shows that with the increase in degradation time, the absorbance steadily decreases, and the maximum absorption peak remains at 664 nm. The absorption peak gradually

Table 1. Study on the kinetic rate of each catalyst on MB solution (20mg/L).

Each catalyst	k(min^{-1})	R^2
NH_2-ZIF-8/NCDs(1:4)	0.03633	0.99633
NH_2-ZIF-8/NCDs(1:5)	0.03862	0.97271
NH_2-ZIF-8/NCDs(1:6)	0.02996	0.94169
NH_2-ZIF-8/NCDs(1:7)	0.02095	0.96958

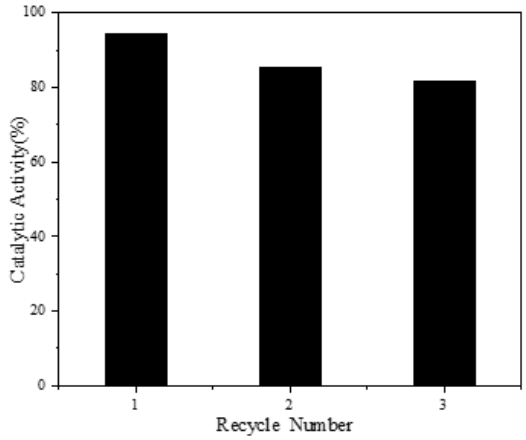

Figure 11. Repeated experiments of MB photodegradation over NH_2-ZIF-8/NCDs composite.

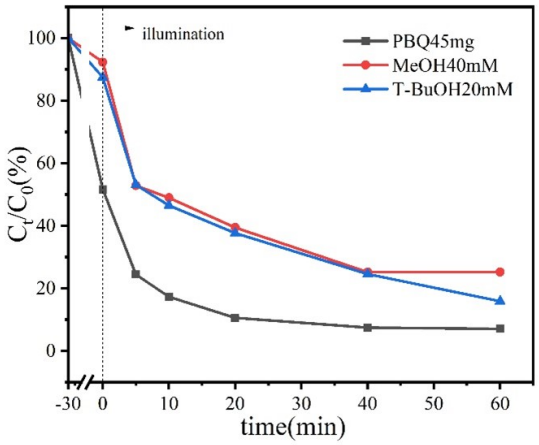

Figure 13. Comparison of the degradation efficiency of NH_2-ZIF-8/NCDs (1:5) on MB solution (20 mg/L) after adding different collectors.

decreases and moves towards the shortwave direction without any new absorption peak, confirming the degradation of MB. The method used in this absorption spectrum is to use dye photosensitivity to extend the light absorption of several semiconductors.

3.4.2 Possible mechanism of photocatalytic activity

Generally, photogenerated holes (h^+), hydroxyl radicals (·OH), and superoxide radicals ($\cdot O^{2-}$) are considered to play a major role in the photocatalytic process. In order to determine the active substances for photocatalytic degradation of organic pollutants, tert-butanol, methanol, and p-benzoquinone were added to 100 mL of MB (20 mg/L) solution before photocatalytic degradation. They were used as free radical trapping agents to capture hydroxyl, hole, and superoxide radicals generated during photocatalytic degradation. As shown in Fig. 13, the degradation rate of MB (20 mg/L) by NH_2-ZIF-8/NCDs without adding a capture agent was 97.1%. After the addition of methanol (40 mM), tert-butanol (20 mM), and p-benzoquinone (45 mg), the degradation rate decreased compared to before. Especially after adding methanol, the degradation rate was only 60%, indicating that hydroxyl radical (·OH) plays a more important role in photocatalytic degradation.

For heterogeneous photocatalytic systems, under appropriate illumination, the electrons in the valence band (VB) of the photocatalyst will be excited to transition to the conduction band (CB), leaving relatively stable electrons in the valence band (VB)-holes (h^+), thus forming electron-hole pairs (e^-/h^+) [42]. Part of these electron-hole pairs generates a strong redox potential, and the other part is recombined and deactivated. The surface of NH_2-ZIF-8/NCDs photocatalyst has a loose and porous structure with a large number of defects, which can effectively capture electrons and holes (e^-/h^+) and prevent the recombination of electrons and holes (e^-/h^+)… As a photosensitizer, NCDs can accelerate the transfer of electrons and increase the migration rate of photocarriers. Oxidation of OH^-/H_2O by h_{VB^+} generates ·OH radicals [43]. Active species include h^+, $\cdot O_{2-}$, and ·OH, which are responsible for the complete degradation of MB pollutants [44]. Among them, ·OH radicals play a key role in degrading MB solution, which is the main reason for the improved photocatalytic activity of NH_2-ZIF-8/NCDs.

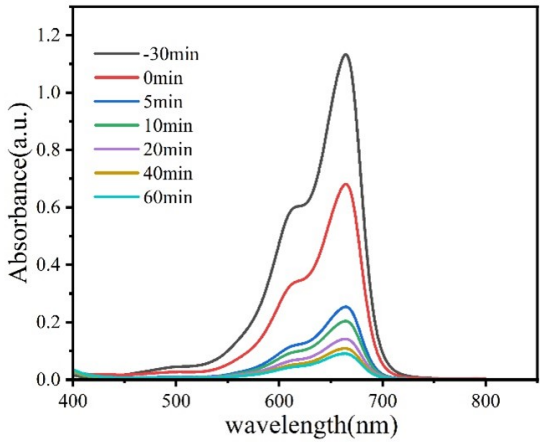

Figure 12. Absorption spectra of 20 mg/L MB solution in the presence of 50 mg NH2-ZIF-8/NCDs.

4. Conclusion

ZIF-8 was aminated and doped with carbon dots through a one-step synthesis method to obtain NH_2-ZIF-8/NCDs photocatalysts. It was observed that adding ethylenediamine for amine modification changed the structure of ZIF-8 to a porous structure and increased the reaction sites of the catalyst. Adding NCDs led to good upconverted fluorescence properties and charge separation efficiency. The photocatalytic activity of ZIF-8, ZIF-8/NCDs, and NH_2-

ZIF-8/NCDs catalysts for degrading MB dye-contaminated water under light irradiation were compared. It was found that the NH_2-ZIF-8/NCDs catalyst has better photocatalytic performance, which can increase the degradation efficiency of methylene blue dye from 48% to 97.1% within 60 minutes. The catalyst exhibits excellent photocatalytic performance. Radical trapping experiments showed that hydroxyl radicals (·OH) are the main active substance responsible for removing MB under light irradiation.

Acknowledgments
The support from the School of Chemical Engineering of Zhengzhou University is gratefully acknowledged.

Authors Contributions
All authors have contributed equally to prepare the paper.

Availability of Data and Materials
The data that support the findings of this study are available from the corresponding author upon reasonable request.

Conflict of Interests
The authors declare that they have no known competing financial interests or personal relationships that could have appeared to influence the work reported in this paper.

References

[1] S. Varjani, P. Rakholiya, H.Y. Ng, S. M. You, and J.A. Teixeira. *Bioresour.Technol*, **314** (2020):123728. DOI: https://doi.org/10.1016/j.biortech.2020.123728.

[2] V. Selvaraj, T.S. Karthika, C. Mansiya, and M. Alagar. *J. Mol. Struct*, **1224** (2021):129195. DOI: https://doi.org/10.1016/j.molstruc.2020.129195.

[3] M. Rezaei and A. Nezamzadeh-Ejhieha. *J. Hydrogen Energy*, **45**(2020):24749–24764. DOI: https://doi.org/10.1016/j.ijhydene.2020.06.258.

[4] A. Yousefi and A. Nezamzadeh-Ejhieh. *Iran. J. Catal*, **11**(2021):247–259.

[5] K.Z. Qi, B. Cheng, J.G. Yu, and W.K. Ho. *Chinese J. Catal*, **38**(2017):1936–1955. DOI: https://doi.org/10.1016/S1872-2067(17)62962-0.

[6] Z. Wei, J. Liu, and W. Shangguan. *Chinese J. Catal*, **41** (2020):1440–1450. DOI: https://doi.org/10.1016/S1872-2067(19)63448-0.

[7] T.Fu, Q.Gao, F. Liu, H. Dai, and X. Kou. *Chinese J. Catal*, **31**(2010):797–802. DOI: https://doi.org/10.3724/SP.J.1088.2010.91220.

[8] X. Zhao, H. Yang, P. Jing, W. Shi, G. Yang, and P. Cheng. *small*, **13**(2017):1603279. DOI: https://doi.org/10.1002/smll.201603279.

[9] D.H. Hong, H.S. Shim, J. Ha, and H.R. Moon. *Korean Chem. Soc*, **42**(2021):956–969. DOI: https://doi.org/10.1002/bkcs.12335.

[10] W. Wang, X. Xu, W. Zhou, and Z. Shao. *Adv. Sci*, **4** (2017):1600371, . DOI: https://doi.org/10.1002/advs.201600371.

[11] H. Furukawa, K.E. Cordova, M.O Keeffe, and O.M. Yaghi. *Science*, **341**(2013):1230444. DOI: https://doi.org/10.1126/science.1230444.

[12] M.A. Nasalevich, M. Van der Veen, and F. Kapteijn. *J. Gascon, Crystengcomm*, **16**(2014):4919–4926. DOI: https://doi.org/10.1039/C4CE00032C.

[13] Y. Li, X. Zhang, A. Yang, C. Jiang, G. Zhang, J. Mao, and Q. Meng. *J. Membr. Sci*, **635**(2021):119521, . DOI: https://doi.org/10.1016/j.memsci.2021.119521.

[14] A. Elaouni, M. EI Ouardi, M. Zbair, A. BaQais, M. Saadi, and H. Ait Ahsaine. *Rsc Adv*, **12**(2022):3181–31817. DOI: https://doi.org/10.1039/D2RA05717D.

[15] M.T. Thanh, T.V. Thien, P.D. Du, N.P. Hung, and D.Q. Khieu. *J. Porous Mater*, **25**(2018):857–869. DOI: https://doi.org/10.1007/s10934-017-0498-7.

[16] H. Jing, C. Wang, Y. Zhang, P. Wang, and R. Li. *Rsc Adv*, **4**(2014):54454–54462. DOI: https://doi.org/10.1039/C4RA08820D.

[17] H. Dai, X. Yuan, L. Jiang, H. Wang, J. Zhang, J.J. Zhang, and T. Xiong. *Coord. Chem. Rev*, **441**(2021):213985. DOI: https://doi.org/10.1016/j.ccr.2021.213985.

[18] Z. Li and J. Li. *Crystengcomm*, **25**(2023):2064–2074. DOI: https://doi.org/10.1039/D2CE01700H.

[19] R. Chandra, S. Mukhopadhyay, and M. Nath. *Mater. Lett*, **164**(2016):571–574. DOI: https://doi.org/10.1016/j.matlet.2015.11.018.

[20] M. Rezaei, A. Nezamzadeh-Ejhieh, and A.R. Massah. *Ecotoxicol. Environ. Saf*, **269**(2024):115927. DOI: https://doi.org/10.1016/j.ecoenv.2024.115927.

[21] W.D.C. Santos, M.M. Teixeira, I.R. Campos, R.B.De Lima, A Mantilla, J.A.Osajima, A.S.De Menezes, D.Manzani, A. Rojasf, and A.C.S. Alcantara. *Microporous Mesoporous Mat*, **359**(2023):112657. DOI: https://doi.org/10.1016/j.micromeso.2023.112657.

[22] Y. Sun, Z. Zhang, A. Xie, C. Xiao, S. Li, F. Huang, and Y. Shen. *Nanoscale*, **7**(2015):13974–13980. DOI: https://doi.org/10.1039/C5NR03402G.

[23] C. Duan, Y. Feng, Y. Xie, M. Ding, and J. Yao. *Microporous Mesoporous Mat*, **347** (2023):112351. DOI: https://doi.org/10.1016/j.micromeso.2022.112351.

[24] J. Jia, C. Jiang, X. Zhang, P. Li, J. Xiong, Z. Zhang, T. Wu, and Y. Wang. *Appl. Surf. Sci*, **495**(2019):143524. DOI: https://doi.org/10.1016/j.apsusc.2019.07.266.

[25] M. Jayasree, A. Asif, N.G. Pillai, K. Archana, and G.T. Prakash. *Mater. Today: Proc*, **41**(2021):564–569. DOI: https://doi.org/10.1016/j.matpr.2020.05.25.

[26] A.A. Abd El Khalk, M.A. Betiha, A.S. Mansour, M.G. Abd El Wahed, and A.M.Al-Sabagh. *Acs Omega*, **6**(2021):26210–26220. DOI: https://doi.org/10.1021/acsomega.1c03195.

[27] C. Zhang, H. Zhang, Y. Yu, S. Wu, and F. Chen. *Talanta*, **197**(2019):451–456. DOI: https://doi.org/10.1016/j.talanta.2019.01.062.

[28] M. Miao, L. Mu, S. Cao, Y. Yang, and X. Feng. *Carbohydr. Polym*, **291**(2022):119587. DOI: https://doi.org/10.1016/j.carbpol.2022.119587.

[29] R. Behnood and G. Sodeifian. *J. Environ. Chem. Eng*, **8**(2020):103821. DOI: https://doi.org/10.1016/j.jece.2020.103821.

[30] T. Tang, C. Lia, W. He, W. Hong, H. Zhua, G. Liu, Y. Yua, and C. Lei. *J. Alloy. Compd*, **894**(2022):162559. DOI: https://doi.org/10.1016/j.jallcom.2021.162559.

[31] N. A. H. M. Nordin, S. M. Racha, T. Matsuura, N. Misdan, N. A. A. Sani, A. F. Ismail, and A. Mustafa. *RSC Adv*, **5**(2015):43110–43120. DOI: https://doi.org/:10.1039/C5RA02230D.

[32] Y. M. He, L. Zeng, Zh. Feng, Q. L. Zhang, X. Y. Zhao, S. F. Ge, X. Hu, and H. J. Lin. *Adv Powder Technol*, **31.1** (2020):439–447. DOI: https://doi.org/10.1016/j.apt.2019.11.002.

[33] H. Ma, Z. Wang, X.-F. Zhang, M. Ding, and J. Yao. *Carbonhyd. Polym*, **270** (2021):118376. DOI: https://doi.org/10.1016/j.carbpol.2021.118376.

[34] L.Z. Cheong, Y. Wei, H. Wang, Z. Wang, X. Su, and C. Shen. *J. Nanoparticle Res*, **19**(2017):280. DOI: https://doi.org/10.1007/s11051-017-3979-3.

[35] L.Y. Wang, M.Q. Fang, J. Liu, J. He, L.H. Deng, J.D. Li, and J. D. Lei. *RSC Adv*, **5**(2015):50942, . DOI: https://doi.org/10.1039/C5RA06185G.

[36] Y. Si, X. Li, G. Yang, X. Mie, and L. Ge. *J Mater Sci*, **55**(2020):13049–13061. DOI: https://doi.org/10.1007/s10853-020-04909-8.

[37] R. Li, W. Li, Ch. Jin, Q.Y. He, and Y.Z. Wang. *J. Alloys Compd*, **825**(2020):154008, . DOI: https://doi.org/10.1016/j.jallcom.2020.154008.

[38] T.T.B. Quyen, P.H. Dang, N.N.T. My, D.T. Pham, D.V. Hong Thiena, and L.H. Vu Thanh. *Iran. J. Catal*, **12** (2022):85–95.

[39] V.D. Dang, T. Annadurai, A.P. Khedulkar, J. Lin, J. Adorna, W. Yu, B. Pandit, T.V. Huynh, and R. Doong. *Appl. Catal. B*, **320**(2023):121928. DOI: https://doi.org/10.1016/j.apcatb.2022.121928.

[40] A.T. Gu, J.Y. Chen, Q.H. Gao, M.M. Khan, P. Wang, Y. Jiao, Z. X. Zhang, Y. Liu, and Y. Yang. *Appl. Surf. Sci*, **516**(2020):146160. DOI: https://doi.org/10.1016/j.apsusc.2020.146160.

[41] N. Chang, Y.R. Chen, F. Xie, Y.P. Liu, and H.T. Wang. *Colloid Surface A*, **616**(2021):126351. DOI: https://doi.org/10.1016/j.colsurfa.2021.126351.

[42] T. Seyedi-Chokanlou, S. Aghabeygi, N. Molahasani, and F. Abrinaei. *Iran. J. Catal*, **11(1)**(2021):49–58.

[43] E. Zarei. *Iran. J. Catal*, **9(2)**(2019):99–108.

[44] B.M. Pirzada, N.A. Mir, N. Qutub, O. Mehraj, S. Sabir, and M. Muneer. *Mater. Sci.Eng: B*, **193**(2015):137–145. DOI: https://doi.org/10.1016/j.mseb.2014.12.005.